arXiv:1210.0195v1 [hep-ph] 30 Sep 2012

Searching for the signal of dark matter and photon associated production at the LHC beyond leading order

Fa Peng Huang,[1] Chong Sheng Li*,[1,2] Jian Wang,[1] and Ding Yu Shao[1]

[1]*Department of Physics and State Key Laboratory of Nuclear Physics and Technology,*
Peking University, Beijing, 100871, China
[2]*Center for High Energy Physics, Peking University, Beijing, 100871, China*

Abstract

We study the signal of DM and photon associated production induced by the dimension six vector and axial-vector operators at the LHC, including the QCD next-to-leading-order (NLO) corrections. We find that the QCD NLO corrections reduce the dependence of the total cross sections on the factorization and renormalization scales, and the K-factors increase with the increasing of the DM mass, which can be as large as about 1.3 for both the vector and axial-vector operators. Using our QCD NLO results, we improve the constraints on the new physics scale from the results of recent CMS experiment. Moreover, we show the Monte Carlo simulation results for detecting the $\gamma + \not{E}_T$ signal at the QCD NLO level, and present the integrated luminosity needed for a 5σ discovery at the LHC with $\sqrt{S} = 14$ TeV. If the signal is not observed, the lower limit on the new physics scale can be set.

PACS numbers: 12.38.Bx, 14.65.Jk, 14.70.Bh, 95.35.+d

---

* Electronic address: csli@pku.edu.cn

I. INTRODUCTION

The dark matter (DM) attracts a lot of attention in the fields of both cosmology and particle physics [1, 2]. The astrophysical observations have provided strong evidence for the existence of DM [3]. The relic abundance of DM favors the weakly interacting massive particles and this kind of DM has been extensively studied. Since there are no DM candidates in the Standard Model (SM), any discovery of the DM signal implies new physics (NP) beyond the SM.

There are mainly three kinds of methods to detect the DM. First, we can detect DM annihilation signals from galaxy clusters, such as PAMELA [4], ATIC [5], HESS [6] and Fermi-LAT [7, 8]. Second, we can search for the signal of DM underground when the DM particles interact with nuclei, such as the experiments of XENON [9], CDMS [10], DAMA [11] and CoGeNT [12]. Third, we can study the properties of DM at hadron colliders if DM exists and has interactions with the SM particles [13, 14]. Compared to the direct and indirect experiments, the hadron colliders have impressive advantages that the measurements are not sensitive to the uncertainties related to the galactic distributions, DM velocities, etc. There have been a lot of studies to search for DM at the LHC in a series of DM models [15–32].

At the LHC, the DM manifests itself as missing energy when produced. However, we can probe the DM through the visible particles, which are associated produced, such as a photon or a jet [33, 34]. In this work, we only consider the DM and photon associated production at the LHC, since this signal is clear and suffers from less backgrounds from the SM. Since the fundamental theory of the DM is unknown, it is useful to investigate the DM in a model-independent way by using effective field theory.

Recently, the CMS collaboration has searched for NP in the $\gamma + \not{E}_T$ final state, and set the 90% confidence level (CL) lower limits on the NP scale for vector and axial-vector operators [13]. However, the analysis there is based on the leading order (LO) results, which suffer from large uncertainties due to the choice of renormalization and factorization scales. Following our previous works [35, 36], in this paper, we study the signal of DM and photon associated production induced by the dimension six vector and axial-vector operators at the LHC, including QCD next-to-leading-order (NLO) corrections. Using our NLO results, we improve the constraints on the NP scale from the results of recent CMS experiment.

The paper is organized as follows. In Sec. II, we describe the dimension six vector and axial-vector operators describing the interactions between DM and the SM particles. In Sec. III, we calculate the relic abundance induced by these effective operators and find the allowed regions for the mass and coupling of the DM. In Sec. IV, we present the details of the QCD NLO corrections to the associated production of the DM and photon at the LHC. In Sec. V, we discuss the scale dependence and show the QCD NLO cross sections for different DM masses numerically. After that we improve the experimental constraints given by CMS collaboration. In Sec. VI, we calculate the backgrounds in the SM and analyze the discovery potential at the LHC with $\sqrt{S} = 14$ TeV. Finally, we conclude in Sec. VII.

II. EFFECTIVE OPERATOR

We consider the dimension six vector and axial-vector operators

$$\begin{aligned} \mathcal{O}_V &= \frac{\kappa}{\Lambda^2}(\bar{q}\gamma^\mu q)(\bar{\chi}\gamma_\mu\chi), \\ \mathcal{O}_A &= \frac{\kappa}{\Lambda^2}(\bar{q}\gamma^\mu\gamma_5 q)(\bar{\chi}\gamma_\mu\gamma_5\chi), \end{aligned} \tag{1}$$

which are also studied in Refs. [25, 33, 37, 38]. The NP scale Λ can be regarded as the remnant of integrating the massive propagator between the DM and SM particles. We assume that the Dirac fermion χ is a DM candidate, and a singlet under the SM gauge group $SU(3)_c \times SU(2)_L \times U(1)_Y$. The DM χ can only interact with the quarks by these operators. In Ref. [13], the constraints on the NP scale Λ are given by the CMS collaboration through the process of DM and photon associated production at LO. In this paper, we will perform the QCD NLO corrections to these processes, whose effects are important for research at the LHC, and improve the limits on the NP scale. For simplicity, we only present the details of the calculations for the vector operator. For the axial operator, we only give some necessary analytical results and the numerical results. The Feynman diagrams are the same for both vector operators and axial-vector operators except for the vertices.

III. RELIC ABUNDANCE

Before discussing the signal of the DM at the LHC, we first consider the relic abundance which is a precise observable in cosmology. The DM we choose to study can contribute to

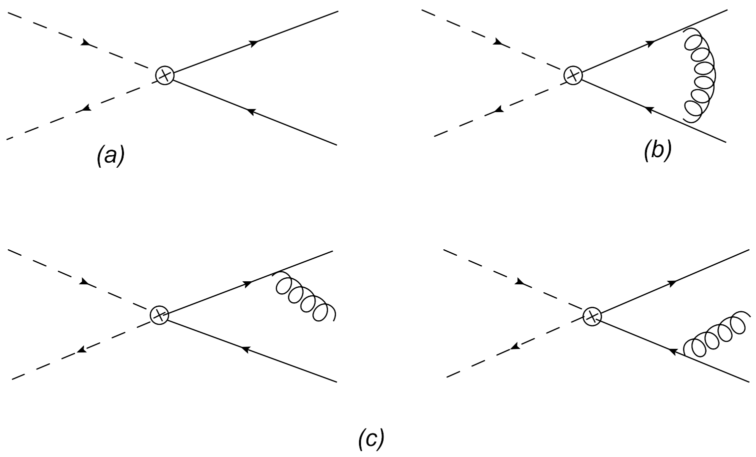

FIG. 1: Feynman diagrams for the DM annihilation process. Labels (a), (b) and (c) denote the LO, virtual correction and real corrections, respectively.

the relic abundance of cold dark matter (CDM). Therefore, the relic abundance imposes constraints on the DM. Here we use the experimental results for the relic abundance in Ref. [39]

$$\Omega_{CDM}h^2 = 0.1123 \pm 0.0035, \tag{2}$$

where Ω_{CDM} is the CDM energy density of the universe normalized by the critical density and $h = 0.710 \pm 0.025$ is the scaled Hubble parameter.

The relic abundance can be calculated from the total annihilation cross section of DM, for which the Feynman diagrams are shown in Fig. 1. First, we give the LO total annihilation cross section for the vector operator

$$\sigma^{an}_{B,V} = N_c N_f \frac{\kappa^2}{\Lambda^4}\sqrt{\frac{s}{s-4m^2}}\frac{s+2m^2}{12\pi}, \tag{3}$$

where s is the usual Mandelstam variable. N_c and N_f are the numbers of color and flavor of quarks, respectively. m is the mass of the DM. This LO cross section is consistent with the result in Ref. [37].

The QCD NLO corrections to the total annihilation cross section include two parts, i.e., the one-loop virtual corrections and real gluon emission corrections. We use $n = 4 - 2\epsilon$ dimensional regularization to regulate the divergences in the calculation. The results of virtual corrections are

$$\sigma^{an}_{v,V} = \sigma^{an}_{B,V}\left(\frac{\alpha_s C_F}{2\pi}\right) D_\epsilon \left(-\frac{2}{\epsilon^2} - \frac{3}{\epsilon} - 8\right), \tag{4}$$

where $D_\epsilon = (4\pi\mu^2/s)^\epsilon \frac{\Gamma(1-\epsilon)^2}{\Gamma(1-3\epsilon)}$ and $C_F = 4/3$. The results of real corrections are

$$\sigma^{an}_{r,V} = \sigma^{an}_{B,V} \left(\frac{\alpha_s C_F}{2\pi}\right) D_\epsilon \left(\frac{2}{\epsilon^2} + \frac{3}{\epsilon} + \frac{19}{2}\right). \tag{5}$$

Combining the two parts, we get the QCD NLO total annihilation cross section

$$\sigma^{an}_{NLO,V} = K^{an} \sigma^{an}_{B,V}, \tag{6}$$

in which K^{an} is the K-factor, generally defined as $\sigma_{\rm NLO}/\sigma_{\rm LO}$, of the DM annihilation cross section

$$K^{an} = 1 + \frac{\alpha_s}{\pi}. \tag{7}$$

The DM is moving at nonrelativistic velocities ($v \ll 1$) when freezing out. We define v as the relative velocity between the DM. Thus we can expand

$$\sigma^{an}_{NLO,V} v = a + bv^2, \tag{8}$$

where

$$\begin{aligned} a &= K^{an} N_c N_f \frac{\kappa^2}{\Lambda^4} \frac{m^2}{\pi}, \\ b &= K^{an} N_c N_f \frac{\kappa^2}{\Lambda^4} \frac{7m^2}{24\pi}. \end{aligned} \tag{9}$$

We perform the calculation of relic abundance by using the method in Ref. [40]. The freeze-out epoch $x_f = m/T_f$ is given by

$$\begin{aligned} x_f &= \ln\left[0.038 a m_{Pl} m \left(g/g_*^{1/2}\right)\right] - \frac{1}{2}\ln\left\{\ln\left[0.038 a m_{Pl} m \left(g/g_*^{1/2}\right)\right]\right\} \\ &+ \ln\left\{1 + \frac{6b}{a \ln\left[0.038 a m_{Pl} m \left(g/g_*^{1/2}\right)\right]}\right\}, \end{aligned} \tag{10}$$

where $m_{Pl} = 1.22 \times 10^{19}$ GeV is the Planck mass. g and g_* is the number of relativistic degrees of freedom and effective number of relativistic degrees of freedom at the freeze-out temperature T_f, respectively. The result for the relic abundance is

$$\Omega_\chi h^2 \approx \frac{1.07 \times 10^9 \ \mathrm{GeV}^{-1} x_f}{(g_{*S}/g_*^{1/2}) m_{Pl} a}. \tag{11}$$

For most of the history of the universe all particle species had a common temperature, and g_{*S} can be replaced by g_*. Requiring the DM relic abundance is in the 2σ region around the

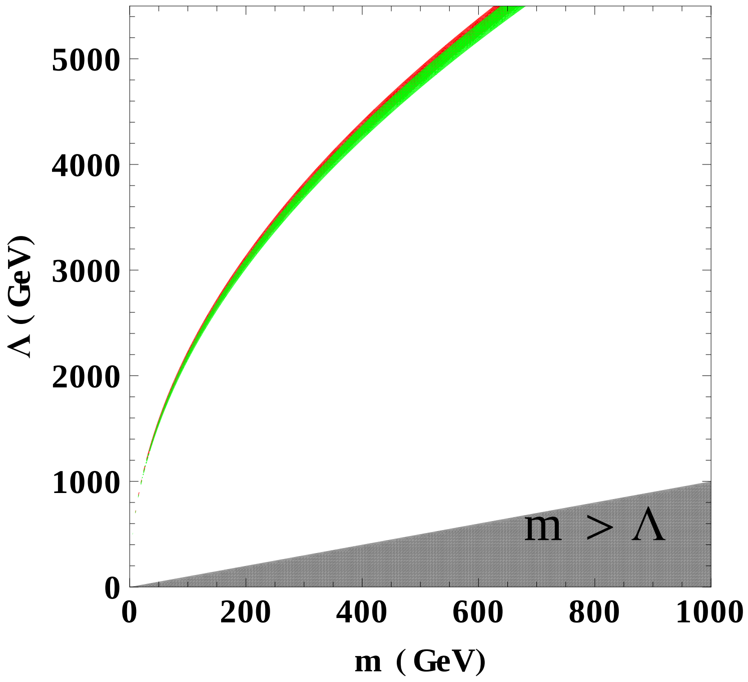

FIG. 2: Relation between the mass of DM and the NP scale for the vector operator. The relic abundance is required be to in the 2σ region around the observed central value. The lower green band is the LO result. The upper red band is the NLO result. In this figure, we choose $\kappa = 1, \alpha_s = 0.118$ and $N_f = 5$.

observed central value, the NP scale of the effective operator is determined by the mass of the DM. From Fig. 2, we see that the NLO corrections increase the lower limits on the NP scale slightly. Since we do not hold the point of view that the relic abundance is determined only by this one kind of DM, the regions below the red band are all allowed.

For the case of axial-vector operator, we follow the same process and give only the main results. The born cross section is

$$\sigma_{B,A}^{an} = N_c N_f \frac{\kappa^2}{\Lambda^4} \sqrt{\frac{s}{s-4m^2}} \frac{s-4m^2}{12\pi}. \tag{12}$$

After taking the QCD NLO corrections to the process induced by the axial-vector operator, we get

$$\sigma_{NLO,A}^{an} v = a + b v^2, \tag{13}$$

in which

$$\begin{aligned} a &= 0, \\ b &= (1+\frac{\alpha_s}{\pi}) N_c N_f \frac{\kappa^2}{\Lambda^4} \frac{m^2}{12\pi}. \end{aligned} \tag{14}$$

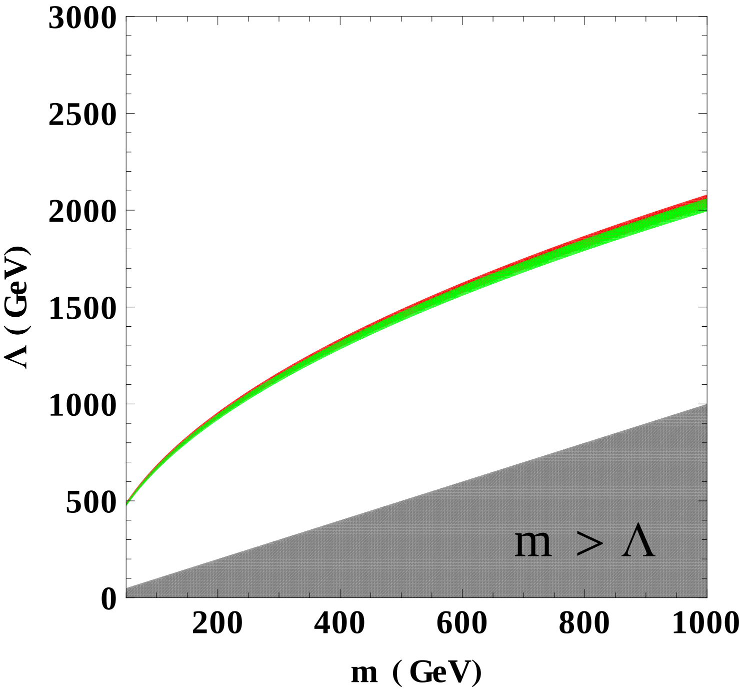

FIG. 3: Relation between the mass of DM and the NP scale for the axial-vector operator. The relic abundance is required be to in the 2σ region around the observed central value. The lower green band is the LO result. The upper red band is the NLO result. In this figure, we choose $\kappa = 1, \alpha_s = 0.118$ and $N_f = 5$.

Then we get the constraints from the relic abundance as shown in Fig. 3 by using the following formulae

$$x_f = \ln\left[0.456 b m_{Pl} m \left(g/g_*^{1/2}\right)\right] - \frac{3}{2}\ln\left\{\ln\left[0.456 b m_{Pl} m \left(g/g_*^{1/2}\right)\right]\right\}, \tag{15}$$

$$\Omega_\chi h^2 \approx \frac{1.07\times 10^9\ \mathrm{GeV}^{-1} x_f^2}{3(g_{*S}/g_*^{1/2}) m_{Pl} b}. \tag{16}$$

From Fig. 3, we get nearly the same results that the NLO corrections increase the lower limits on the NP scale slightly, and the regions below the red band are all allowed.

IV. QCD NLO CORRECTIONS TO DM AND PHOTON ASSOCIATED PRODUCTION

From the effective operators in Eq. (1), the DM can be pair produced via annihilation of quark pairs. However, because DM can not decay into SM particles, such processes give just

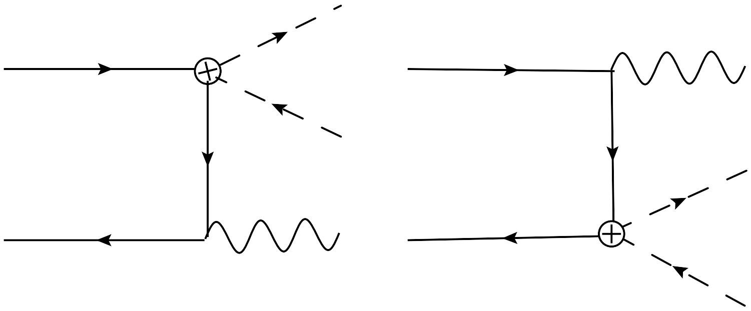

FIG. 4: LO Feynman diagrams of the DM and photon associated production.

missing energy and no observable signals. As a result, we have to consider the process of DM associated production with a photon or a jet [25, 33, 38] and use the initial radiation to tag the DM. Though the cross section of associated production with a photon is less than that of associated production with a jet, the signal of this process is characteristic and involves less backgrounds.

Different from the scalar operator in our previous work [35], the quark sector and the DM sector can not factorize for the vector and axial-vector operators that we consider in this paper. This leads to more complicated analytical expressions in our calculation. We only show the analytical results for the vector operator in detail and give the numerical results for both of the vector and axial-vector operators.

A. LO calculation

First of all, we calculate the LO cross section of the following process

$$q(p_1) + \bar{q}(p_2) \to \chi(p_3) + \bar{\chi}(p_4) + \gamma(p_5). \tag{17}$$

The LO Feynman diagrams are shown in Fig. 4. Then the LO partonic cross section is

$$\hat{\sigma}_B = \frac{1}{2s_{12}} \int d\Gamma_3 \overline{|\mathcal{M}_B|^2}, \tag{18}$$

in which Γ_3 is the three-particle final states phase space. We define $s_{ij} = (p_i + p_j)^2$, $t_{ij} = (p_i - p_j)^2$ and $\alpha = e^2/4\pi$. The spin and color summed and averaged Born matrix element squared is

$$\overline{|\mathcal{M}_B|^2} = \frac{\pi\alpha\kappa^2}{3\Lambda^4} \sum_i Q_i^2 |\mathcal{M}_0^{V(A)}|^2, \tag{19}$$

in which $|\mathcal{M}_0^V|^2$ is expressed as

$$\begin{aligned}
|\mathcal{M}_0^V|^2 \ = \ & \frac{1}{t_{15}t_{25}}16(2m^4(4s_{12}+t_{15}+t_{25})+m^2(-s_{12}(2s_{35} \\
& +2s_{45}+3t_{13}+3t_{14}-4t_{15}+3t_{23}+3t_{24}-4t_{25}) \\
& -s_{45}t_{15}-s_{45}t_{25}-s_{35}(t_{15}+t_{25})+ \\
& 4(s_{12})^2+2(t_{15})^2+2(t_{25})^2-2t_{13}t_{15}-2t_{14}t_{15}+t_{15}t_{23}+t_{15}t_{24}+ \\
& t_{13}t_{25}+t_{14}t_{25}-2t_{23}t_{25}-2t_{24}t_{25})+s_{45}t_{13}t_{15}+ \\
& s_{35}t_{14}t_{15}+s_{12}(s_{45}(t_{13}+t_{23})+ \\
& s_{35}(t_{14}+t_{24})+2(t_{14}t_{23}+t_{13}t_{24}))+s_{45}t_{23}t_{25}+s_{35}t_{24}t_{25}+ \\
& t_{14}t_{15}t_{23}+t_{13}t_{15}t_{24}-2t_{15}t_{23}t_{24}-2t_{13}t_{14}t_{25}+ \\
& t_{14}t_{23}t_{25}+t_{13}t_{24}t_{25}),
\end{aligned} \tag{20}$$

and $Q_i (i = 1, 5)$ are the electric charge of the quarks. For the axial-vector operator,

$$|\mathcal{M}_0^A|^2 = |\mathcal{M}_0^V|^2 - \frac{64m^2\left(2s_{12}\left(t_{15}+t_{25}\right)+2\left(s_{12}\right)^2+\left(t_{15}\right)^2+\left(t_{25}\right)^2\right)}{t_{15}t_{25}}. \tag{21}$$

After convoluting with the parton distribution functions (PDFs) $G_{q(\bar{q})}(x)$, we obtain the LO cross section

$$\sigma_B = \int dx_1 dx_2 [G_{q/p}(x_1)G_{\bar{q}/p}(x_2) + (x_1 \leftrightarrow x_2)]\hat{\sigma}_B. \tag{22}$$

B. QCD NLO corrections

The QCD NLO corrections consist of real gluon radiation, quark or antiquark emission and one-loop virtual gluon effects. We use $n = 4-2\epsilon$ dimensional regularization to regulate both the ultraviolet (UV) and the infrared (IR) divergences in our calculations.

The virtual gluon corrections involve the self-energy, vertex and box diagrams, as shown in Fig. 5. We use on-shell renormalization scheme for external fields. The UV divergences are exactly canceled between the loop diagrams and the counterterms of the external fields. For the vector operator in our case, there is no renormalization for the new coupling in this renormalization scheme, same as the Drell-Yan process. We denote the bare and renormalized quark wave functions by ψ_{q0} and ψ_q, respectively. The renormalization constant δZ_q is then defined by

$$\psi_{q0} = (1+\delta Z_q)^{1/2}\psi_q. \tag{23}$$

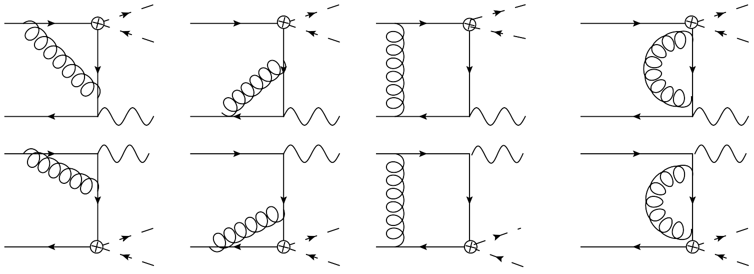

FIG. 5: Feynman diagrams for one-loop virtual corrections.

Calculating the quark self-energy diagram, we obtain the explicit expression for δZ_q:

$$\delta Z_q = \frac{\alpha_s}{4\pi} C_F \left(\frac{1}{\epsilon} - \frac{1}{\epsilon_{UV}} \right) . \tag{24}$$

Here $1/\epsilon$ and $1/\epsilon_{UV}$ represent IR and UV divergences, respectively.

After renormalization, the UV divergences in the virtual corrections are removed, leaving the IR divergences and the finite terms. The final virtual gluon corrections to the partonic cross section are

$$\hat{\sigma}_v = \frac{1}{2s_{12}} \int d\Gamma_3 2\overline{Re(\mathcal{M}_B^* \mathcal{M}_v)}. \tag{25}$$

The IR divergent part of $\mathcal{M}_v$ is given by

$$\mathcal{M}_v^{IR} = \frac{\alpha_s}{4\pi} C_\epsilon \left(\frac{A_2^v}{\epsilon^2} + \frac{A_1^v}{\epsilon^1} \right) \mathcal{M}_B, \tag{26}$$

where $C_\epsilon = \Gamma(1+\epsilon)[(4\pi\mu_R^2)/s_{12}]^\epsilon$ and

$$\begin{aligned} A_2^v &= -2C_F, \\ A_1^v &= -3C_F. \end{aligned} \tag{27}$$

Another possible contribution at hadron collider arises from the process

$$g + g \to \chi + \bar{\chi} + \gamma, \tag{28}$$

which is illustrated in Fig. 6. The effects of these loop-induced gg diagrams are one order of α_s higher than that of $q\bar{q}$ diagrams. The triangle diagrams in Fig.6 vanish because of the color structure. The box diagrams do not vanish, but the gluon PDF is strongly suppressed if we require the final states have large transverse momentum. Thus, we assume their contribution is small and do not discuss this process in the rest of this paper.

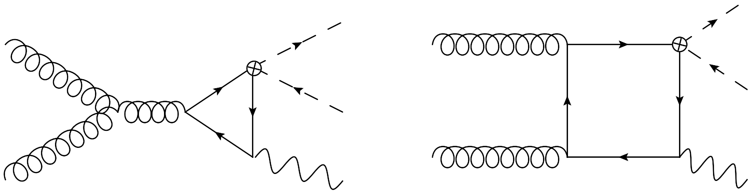

FIG. 6: Sample Feynman diagrams for gluon-gluon initial states contributions.

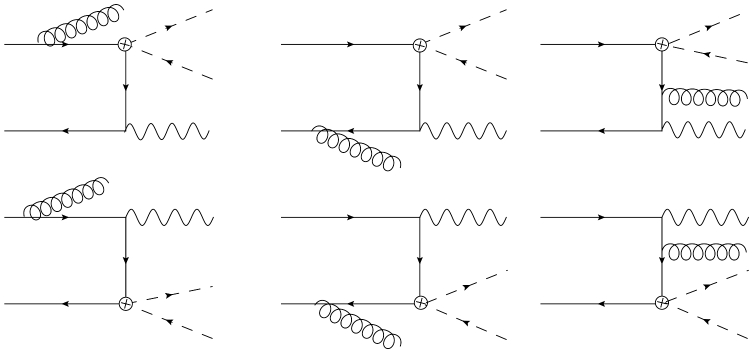

FIG. 7: Feynman diagrams for a real gluon emission.

The Feynman diagrams for the real gluon radiation process

$$q(p_1) + \bar{q}(p_2) \to \chi(p_3) + \bar{\chi}(p_4) + \gamma(p_5) + g(p_6) \tag{29}$$

are shown in Fig. 7. Soft and collinear divergences appear when we perform the final state phase integrations. To cancel the IR singularities, we use the two cutoff phase space slicing method to integrate the singular regions analytically [41]. Explicitly, we use the soft cutoff parameter δ_s to define the soft regions and the collinear cutoff parameter δ_c to define the hard collinear regions. The soft regions are just the phase space where the real radiated gluon's energy $E_6 \leq \delta_s\sqrt{s_{12}}/2$. The collinear regions are defined by $|t_{i6}| < \delta_c s_{12}$ with $i = 1, 2$. Therefore, the real corrections are divided into three parts, i.e.,

$$d\hat{\sigma}_r = d\hat{\sigma}_r^S + d\hat{\sigma}_r^{HC} + d\hat{\sigma}_r^{\overline{HC}}. \tag{30}$$

Here, $\hat{\sigma}_r^S$ and $\hat{\sigma}_r^{HC}$ represent the partonic cross section for the soft regions and hard collinear regions, respectively. The hard non-collinear part $\hat{\sigma}_r^{\overline{HC}}$ is finite and can be computed numerically.

In the soft regions, we use the Eikonal approximation, so that the cross section can be factorized as

$$d\hat{\sigma}_r^S = (4\pi\alpha_s\mu_R^{2\epsilon})d\hat{\sigma}_B \int dS\Phi_{eik}, \tag{31}$$

where the phase space integration factor dS over the soft region is expressed as

$$dS = \frac{1}{2(2\pi)^{3-2\epsilon}} \int_0^{\delta_s \sqrt{s_{12}}/2} dE_6 E_6^{1-2\epsilon} d\Omega_{2-2\epsilon}. \tag{32}$$

And the Eikonal factor Φ_{eik} is the amplitude squared in the soft limit apart from $\overline{|\mathcal{M}_B|^2}$, expressed as

$$\Phi_{eik} = C_F \frac{s_{12}}{t_{16} t_{26}}. \tag{33}$$

After integration over the soft gluon phase space, we get

$$d\hat{\sigma}_r^S = d\hat{\sigma}_B \frac{\alpha_s}{2\pi} C_\epsilon \left(\frac{A_2^S}{\epsilon^2} + \frac{A_1^S}{\epsilon} + A_0^S \right), \tag{34}$$

where

$$A_2^S = 2C_F, \qquad A_1^S = -4C_F \ln \delta_s, \qquad A_0^S = C_F \left(4 \ln^2 \delta_s - \frac{2\pi^2}{3} \right). \tag{35}$$

In hard collinear regions, the momentum of the gluon emitted from initial partons become collinear to the beam line. In this limit, the four-body matrix elements are approximated as follows:

$$\overline{|\mathcal{M}_r|^2} \approx (4\pi\alpha_s \mu_R^2) \overline{|\mathcal{M}_B|^2} \left[\frac{-2P_{qq}(z,\epsilon)}{z t_{16}} + \frac{-2P_{\bar{q}\bar{q}}(z,\epsilon)}{z t_{26}} \right], \tag{36}$$

in which z represents the fraction of initial partons' momentum carried by $q(\bar{q})$. $P_{ij}(z,\epsilon)$ are the unregulated splitting functions in n-dimensions which can be related to the usual Altarelli-Parisi splitting kernels as $P_{ij}(z,\epsilon) = P_{ij}(z) + \epsilon P'_{ij}(z)$. In our case,

$$P_{qq}(z) = C_F \frac{1+z^2}{1-z}, \qquad P'_{qq}(z) = -C_F(1-z). \tag{37}$$

Because of charge conjugation invariance we have

$$P_{\bar{q}\bar{q}} = P_{qq}, \qquad P'_{\bar{q}\bar{q}} = P'_{qq}. \tag{38}$$

At the same limit, the four-body phase space can be written as

$$d\Gamma_4|_{coll} = d\Gamma_3(s'_{12} = z s_{12}) \frac{(4\pi)^\epsilon}{16\pi^2 \Gamma(1-\epsilon)} dz dt_{16} [-(1-z)t_{16}]^{-\epsilon}. \tag{39}$$

Therefore, we obtain

$$\begin{aligned} d\sigma_r^{HC} &= d\hat{\sigma}_B \frac{\alpha_s}{2\pi} C_\epsilon \left(-\frac{1}{\epsilon} \right) \delta_c^{-\epsilon} [P_{qq}(z,\epsilon) G_{q/p}(x_1/z) G_{\bar{q}/p}(x_2) \\ &+ P_{\bar{q}\bar{q}}(z,\epsilon) G_{\bar{q}/p}(x_1) G_{q/p}(x_2/z) + (x_1 \leftrightarrow x_2)] \frac{dz}{z} \left(\frac{1-z}{z} \right)^{-\epsilon} dx_1 dx_2. \end{aligned} \tag{40}$$

To factorize the collinear singularity into the PDFs, we use scale dependent PDFs in the $\overline{\mathrm{MS}}$ convention:

$$G_{b/p}(x,\mu_F) = G_{b/p}(x) + \left(-\frac{1}{\epsilon}\right)\left[\frac{\alpha_s}{2\pi}\frac{\Gamma(1-\epsilon)}{\Gamma(1-2\epsilon)}\left(\frac{4\pi\mu_R^2}{\mu_F^2}\right)^{\epsilon}\right]\int_x^1 \frac{dz}{z}P_{ba}(z)G_{a/p}(x/z). \qquad (41)$$

Now, we replace $G_{q(\bar{q})/p}$ in the LO hadronic cross section (22) and combine the result with the hard collinear contribution in Eq. (40). The resulting $\mathcal{O}(\alpha_s)$ expression for the initial state collinear contribution is

$$\begin{aligned} d\sigma^{coll} &= d\hat{\sigma}_B\frac{\alpha_s}{2\pi}C_\epsilon\Big\{\tilde{G}_{q/p}(x_1,\mu_F)G_{\bar{q}/p}(x_2,\mu_F) + G_{q/p}(x_1,\mu_F)\tilde{G}_{\bar{q}/p}(x_2,\mu_F) \\ &+ \sum_{a=q,\bar{q}}\Big[\frac{A_1^{sc}(a\to ag)}{\epsilon} + A_0^{sc}(a\to ag)\Big]G_{q/p}(x_1,\mu_F)G_{\bar{q}/p}(x_2,\mu_F) \\ &+ (x_1 \leftrightarrow x_2)\Big\}dx_1dx_2. \end{aligned} \qquad (42)$$

with

$$\begin{aligned} A_1^{sc}(q\to qg) &= C_F(2\ln\delta_s + 3/2), \\ A_0^{sc}(q\to qg) &= A_1^{sc}(q\to qg)\ln\Big(\frac{s_{12}}{\mu_F^2}\Big). \end{aligned} \qquad (43)$$

The $\tilde{G}$ functions are given by

$$\tilde{G}_{b/p}(x,\mu_F) = \sum_a\int_x^{1-\delta_s\delta_{ab}}\frac{dy}{y}G_{a/p}(x/y,\mu_F)\tilde{P}_{ba}(y) \qquad (44)$$

with

$$\tilde{P}_{ba}(y) = P_{ba}(y)\ln\Big(\delta_c\frac{1-y}{y}\frac{s_{12}}{\mu_F^2}\Big) - P'_{ba}(y). \qquad (45)$$

A complete real correction includes also the (anti)quark emitted processes, as shown in Fig. 8, such as

$$g(p_1) + q/\bar{q}(p_2) \to \chi(p_3) + \bar{\chi}(p_4) + \gamma(p_5) + q/\bar{q}(p_6). \qquad (46)$$

Their contributions can be obtained from the results of processes in (29) by crossing symmetry. Note that, when separating the singular phase space regions for these processes, one only needs to deal with the collinear divergences which can be totally absorbed into the redefinition of the PDFs in Eq. (41).

Finally, the NLO cross section for the process $pp \to \chi\bar{\chi}\gamma$ is

$$\begin{aligned} \sigma^{NLO} &= \int dx_1dx_2\Big\{\big[G_{q/p}(x_1,\mu_F)G_{\bar{q}/p}(x_2,\mu_F) + (x_1\leftrightarrow x_2)\big](\hat{\sigma}_B + \hat{\sigma}_v + \hat{\sigma}^S + \hat{\sigma}_r^{\overline{HC}})\Big\} + \sigma^{coll} \\ &+ \sum_{a=q,\bar{q}}\int dx_1dx_2\big[G_{g/p}(x_1,\mu_F)G_{a/p}(x_2,\mu_F) + (x_1\leftrightarrow x_2)\big]\hat{\sigma}_r^{\overline{C}}(ga\to\chi\bar{\chi}\gamma a), \end{aligned} \qquad (47)$$

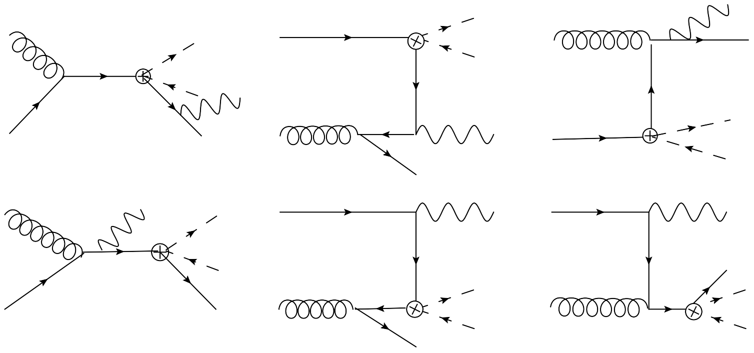

FIG. 8: Feynman diagrams for a quark emission. The Feynman diagrams for antiquark emission can be obtained by charge conjugation.

where $\overline{C}$ in $\hat{\sigma_r}^{\overline{C}}(ga \to \chi\bar{\chi}\gamma a)$ suggests that the phase space integration is performed in the noncollinear regions. We have checked that

$$A_2^v + A_2^S = 0, \qquad A_1^v + A_1^S + 2A_1^{sc}(q \to qg) = 0. \tag{48}$$

Therefore there are no singularities left any more and we can perform numerical integration now.

V. NUMERICAL RESULTS

In this section, we give the numerical results for the cross sections of DM and photon associated production at the LHC. In numerical calculations, we choose the CTEQ6L1 (CTEQ6M) PDF sets [42] and the corresponding strong coupling α_s for the LO (NLO) calculations. The default factorization and renormalization scales, μ_F and μ_R, are set as $2m$. Recently, the observations of the gamma-ray in Fermi-LAT gives the hints of 130 GeV DM [8]. Thus, we choose the input parameters $(m, \Lambda) = (130\text{ GeV}, 500\text{ GeV})$ and $\kappa = 1$ unless otherwise specified, which are allowed by the relic abundance constraint. The kinematic cuts

$$\begin{aligned} p_T^\gamma &> 100\text{ GeV}, \\ |\eta^\gamma| &< 2.4, \\ p_T^{miss} &> 100\text{ GeV}, \end{aligned} \tag{49}$$

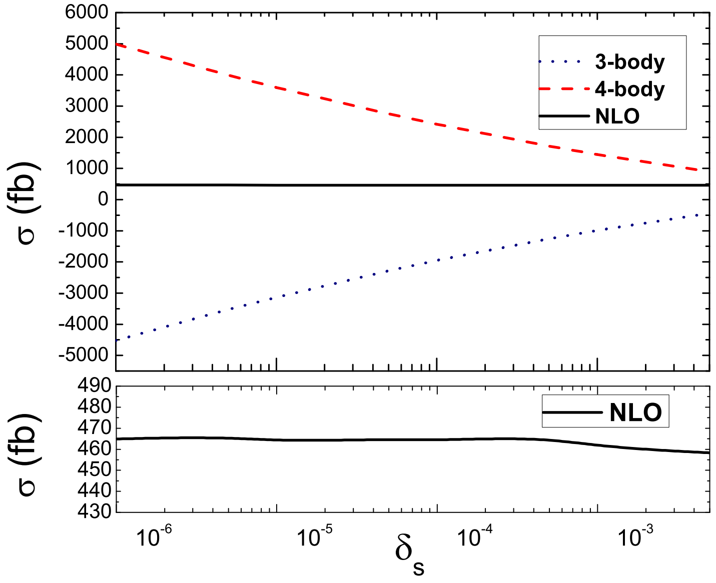

FIG. 9: Dependence of the NLO cross sections for the DM and photon associated production at the LHC on the soft cutoff δ_s with $\delta_c = \delta_s/50$ for the axial-vector operator.

are applied in our numerical calculations. Here p_T^{miss} is the missing transverse momentum, defined as

$$p_T^{miss} \equiv \begin{cases} p_T^{\gamma}, & \text{no jets in the final states,} \\ p_T^{\chi\bar{\chi}}, & \text{with jets in the final states,} \end{cases} \tag{50}$$

where $p_T^{\chi\bar{\chi}}$ is the transverse momentum of the system of the DM. Jets are defined by the requirements $p_T^{jet} > 20$ GeV and $|\eta^{jet}| < 2.5$. In order to avoid QED collinear divergences, we also require the photon to be isolated by the prescription [43]

$$\sum_{R_{j\gamma}\in R_0} p_T^{jet} < p_T^{\gamma}\Big(\frac{1-\cos R_{j\gamma}}{1-\cos R_0}\Big). \tag{51}$$

where $R \equiv \sqrt{\Delta\phi^2 + \Delta\eta^2}$ and $R_0 = 0.4$.

Since we use the two cutoff phase space slicing method in this calculation, it is necessary to show that the total cross section is independent of the cutoff parameter. In Fig. 9, the contribution of three-body final states includes the Born cross section and one-loop virtual corrections, soft and collinear limits of the cross section of four-body final states. The contribution of four-body final states consists in the cross section of four-body final states with the singular regions of the phase space sliced. From Fig. 9, we see that our final result is nearly independent of the cutoff parameter, since the total cross section varies less than

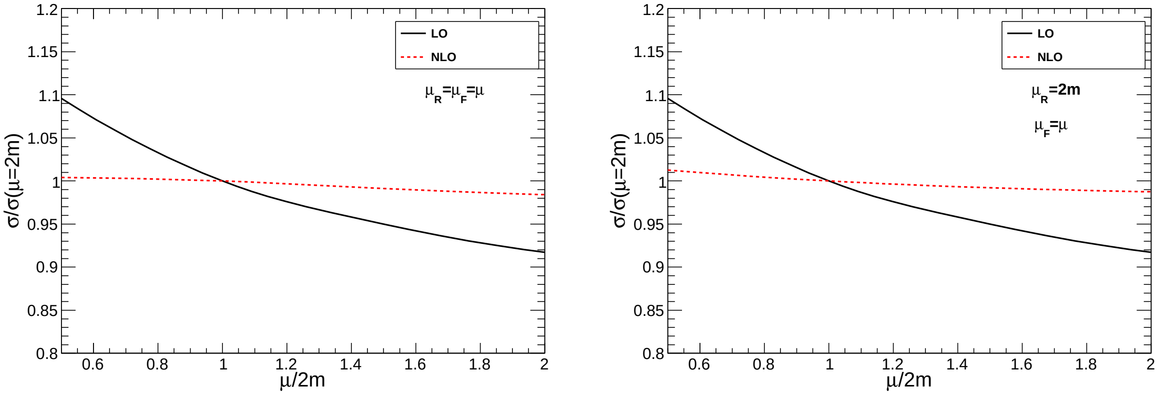

FIG. 10: Dependence of the LO (NLO) cross sections for the DM and photon associated production at the LHC on the factorization scale μ_F and renormalization scale μ_R for the vector operator.

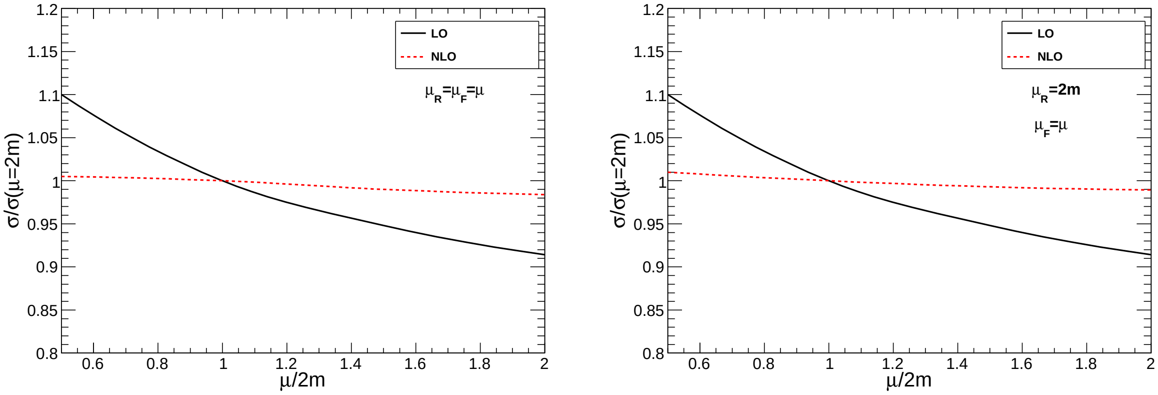

FIG. 11: Dependence of the LO (NLO) cross sections for the DM and photon associated production at the LHC on the factorization scale μ_F and renormalization scale μ_R for the axial-vector operator.

5% when the parameter δ_s changes from 10^{-6} to 0.005.

In Fig. 10 and Fig. 11, we show the dependence of the LO (NLO) cross sections for the DM and photon associated production at the LHC on the factorization scale μ_F and renormalization scale μ_R. It can be seen that the dependence of the NLO cross section on the factorization scale μ_F and renormalization scale μ_R is significantly reduced, compared to the LO cross section. This makes the theoretical prediction much more reliable.

In Fig. 12, we show the DM mass dependence of the LO and NLO cross sections for the vector operator with $\sqrt{S} = 14$ TeV. When the DM mass varies from 130 GeV to 200 GeV, the QCD NLO corrections are modest. For the DM mass in the range from 300 GeV to 1000

GeV, the QCD NLO corrections generally improve the cross section and are more significant for larger DM mass. For example, the QCD NLO corrections increase the cross sections by about 19% for $m = 1000$ GeV. Thus, it is necessary to consider the NLO corrections to the process of DM production at hadron colliders. We also show the mass dependence of the K-factors for the axial-vector operator in Fig. 13, which are similar to the case of vector operator. In order to compare with the experimental results of CMS, we use the same cuts and center-of-mass energy as in [13], and can improve the lower limits on the NP scale in the results of CMS [13], using our K-factors at the LHC with $\sqrt{S} = 7$ TeV. Here, we show the improved limits on the NP scale Λ in Table I and Table II for the vector and axial-vector operators, respectively.

TABLE I: Sample results of the 90% CL lower limits on the NP scale Λ for the vector operator. The LO results are given in the CMS analysis [13]. The K-factors at the LHC with $\sqrt{S} = 7$ TeV for different DM masses are also shown.

m [GeV]	Λ [GeV](LO) [13]	Λ [GeV](NLO)	K-factor@7 TeV
200	549	564	1.11
500	442	463	1.20
1000	246	263	1.31

TABLE II: Sample results of the 90% CL lower limits on the NP scale Λ for the axial-vector operator. The LO results are given in the CMS analysis [13]. The K-factors at the LHC with $\sqrt{S} = 7$ TeV for different DM masses are also shown.

m [GeV]	Λ [GeV](LO) [13]	Λ [GeV](NLO)	K-factor@7 TeV
200	508	517	1.07
500	358	372	1.17
1000	172	183	1.29

VI. BACKGROUNDS AND DISCOVERY POTENTIAL

In this section, we present the Monte Carlo simulation results for detecting the $\gamma + \not{E}_T$ signal at the QCD NLO level. The main irreducible SM backgrounds are the $pp \to Z(\to$

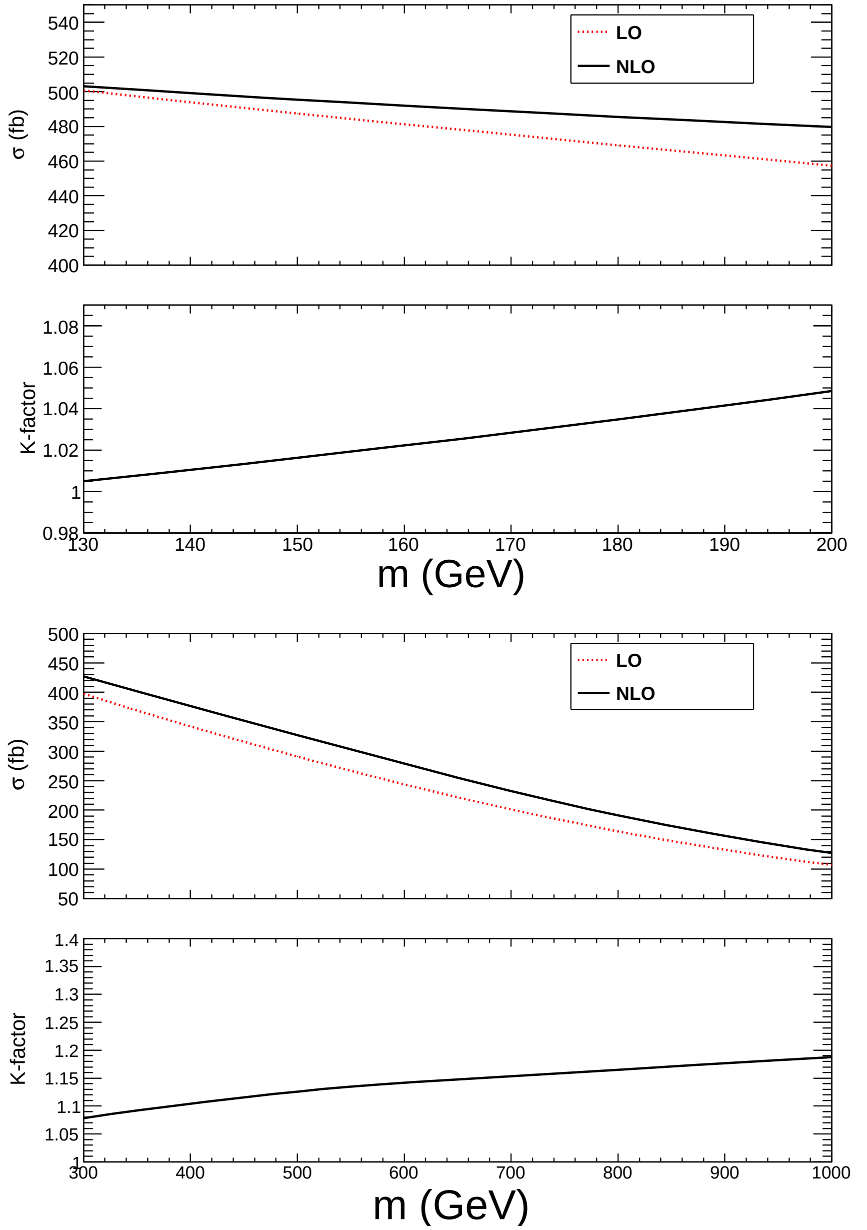

FIG. 12: Dependence of the LO and NLO cross sections on the DM mass for the vector operator with $\sqrt{S} = 14$ TeV. The K-factors are also shown.

$\nu\bar{\nu}) + \gamma$ and $pp \to Z(\to \nu\bar{\nu}) + j$ when the jet is misidentified as a photon. We use MCFM [44–47] to calculate the backgrounds at the NLO level. Since we focus on the experiments at the LHC, we set the missidentified probability $P_{\gamma/j} = 10^{-4}$, as pointed in the Ref. [48].

Figure 14 and Figure 15 show the differential cross sections as functions of p_T^γ and p_T^{miss}, respectively, for the signal and backgrounds at the NLO level. We can see that the distributions of the backgrounds decrease faster than that of the signal as the transverse momentum

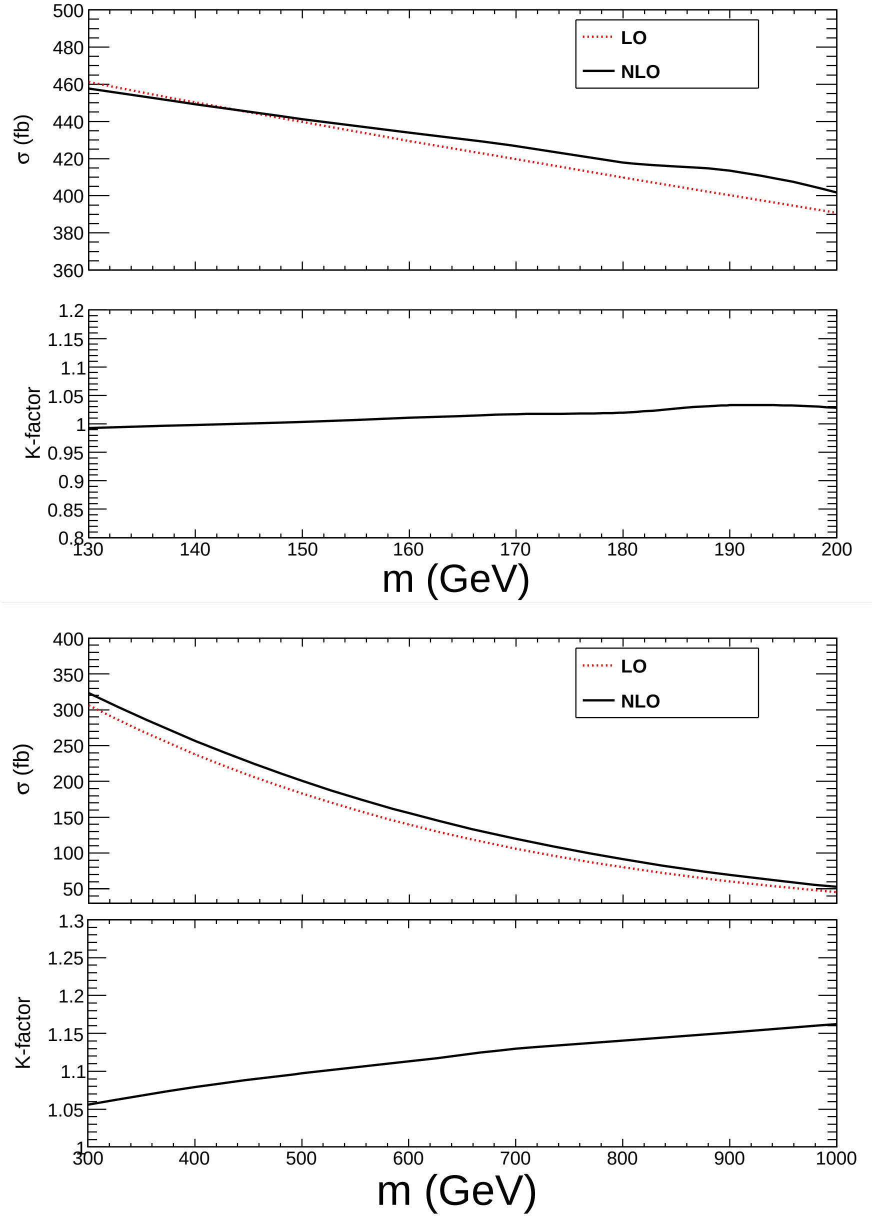

FIG. 13: Dependence of the LO and NLO cross sections on the DM mass for the axial-vector operator with $\sqrt{S} = 14$ TeV. The K-factors are also shown.

of the photon increases. Thus, the ratio of signal and background will increase if we set a larger p_T cut.

Figure 16 shows the differential cross sections as a function of η^{γ} for the signal and the backgrounds at the NLO level. We see that the distribution of the signal is more concentrated in the central region than the backgrounds. These distributions give some clues to suppress

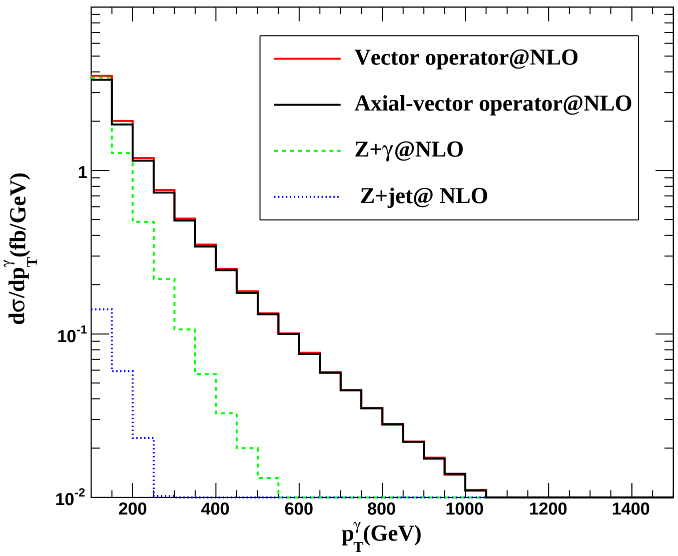

FIG. 14: Dependence of the differential cross section on p_T^γ.

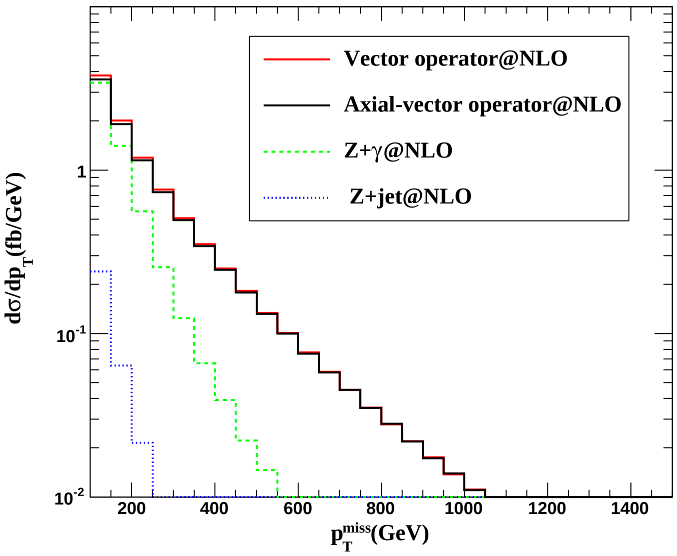

FIG. 15: Dependence of the differential cross section on $p_{\rm T}^{miss}$.

the backgrounds more efficiently at the LHC.

Figure 17 presents the integrated luminosity needed to discover the signal at a 5σ ($\mathcal{S}/\sqrt{\mathcal{S}+\mathcal{B}} = 5$) level at the LHC with $\sqrt{S} = 14$ TeV. We find that the needed integrated luminosity grows with the increasing of the NP scale, and depends more strongly on the DM mass for larger NP scale. In particular, for $\Lambda = 1000$ GeV and $m = 200$ GeV, the

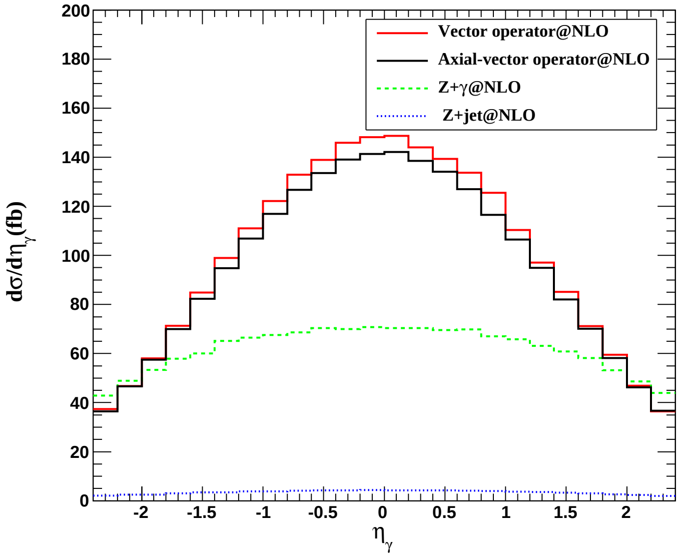

FIG. 16: Dependence of the differential cross section on η^{γ}.

needed integrated luminosity is 12 fb^{-1} at the 14 TeV LHC. Fig. 18 shows the results for the axial-vector operator.

In Fig. 19, we present the limits of the NP scale for 3σ ($\mathcal{S}/\sqrt{\mathcal{B}} = 3$) and 5σ ($\mathcal{S}/\sqrt{\mathcal{B}} = 5$) exclusions at the LHC with $\sqrt{S} = 14$ TeV, assuming $m = 130$ GeV. We see that the NP scale is constrained to be larger than 1200 GeV if the LHC with $\sqrt{S} = 14$ TeV does not detect this signal after collecting an integrated luminosity of 10 fb^{-1}. Figure 20 gives the results for the axial-vector operator.

VII. CONCLUSION

We have investigated the signal of DM and photon associated production induced by the dimension six vector and axial-vector operators at the LHC, including the QCD NLO corrections. We find that the QCD NLO corrections significantly reduce the dependence of the total cross sections on the factorization and renormalization scales, and the QCD NLO corrections are more significant for larger DM mass for both the vector and axial-vector operators. Using our NLO results, we improve the constraints on the NP scale from the results of recent CMS experiment. Moreover, we calculate the dominant SM backgrounds at the NLO level, and show the differential cross sections of both the signal and backgrounds

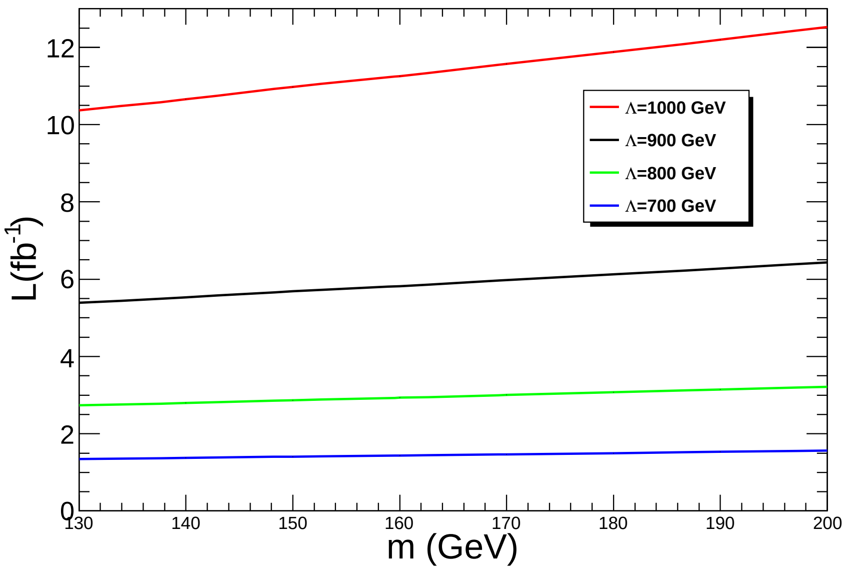

FIG. 17: The integrated luminosity needed for a 5σ discovery as a function of the DM mass at the LHC with $\sqrt{S} = 14$ TeV for vector-operator. We choose the cuts $p_T^{\gamma} > 300$ GeV and $p_T^{miss} > 300$ GeV due to the above analysis of Fig. 14 and Fig. 15.

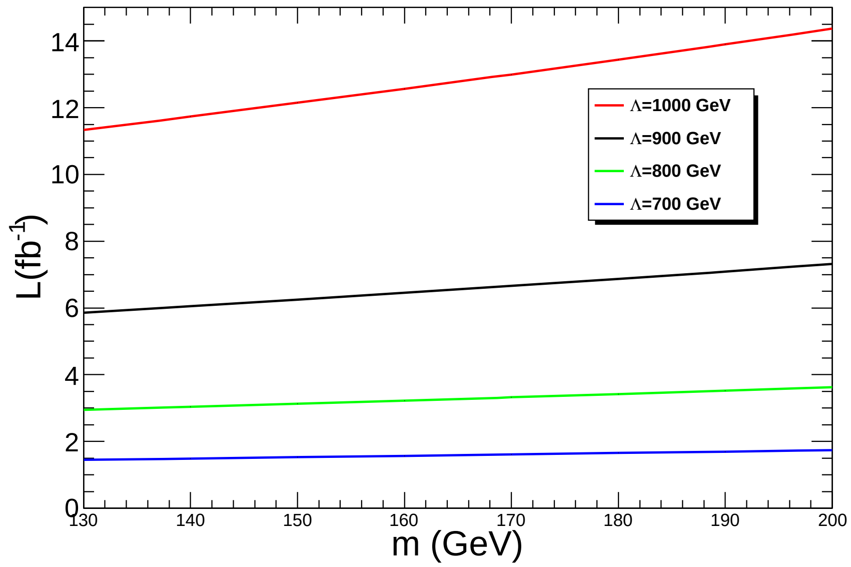

FIG. 18: The integrated luminosity needed for a 5σ discovery as a function of the DM mass at the LHC with $\sqrt{S} = 14$ TeV for axial-vector operator. We choose the cuts $p_T^{\gamma} > 300$ GeV and $p_T^{miss} > 300$ GeV due to the above analysis of Fig. 14 and Fig. 15.

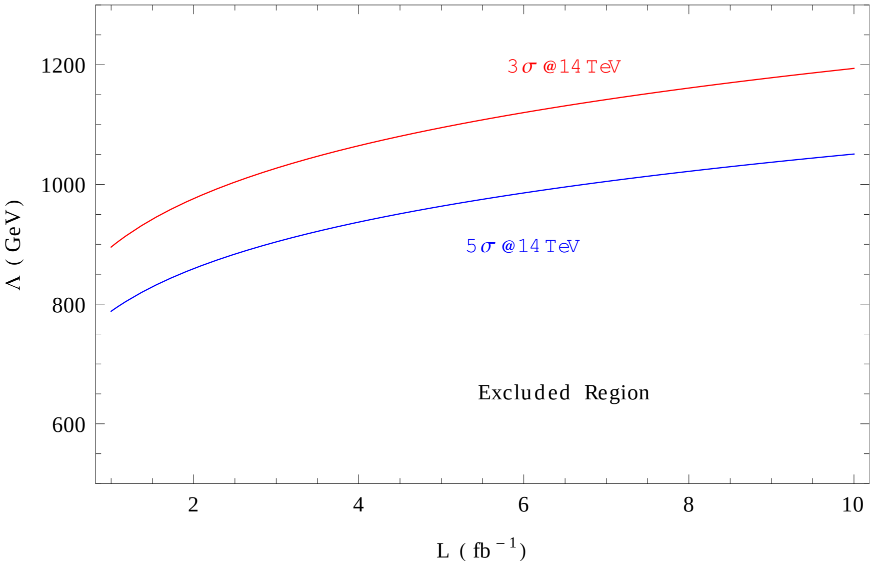

FIG. 19: The limits of the NP scale for 3σ and 5σ exclusions at the LHC with $\sqrt{S} = 14$ TeV, assuming $m = 130$ GeV for the vector operator. We choose the cuts $p_T^\gamma > 300$ GeV and $p_T^{miss} > 300$ GeV due to the above analysis of Fig. 14 and Fig. 15.

as functions of $p_{\rm T}^\gamma$, $p_{\rm T}^{\rm miss}$ and η^γ. The character of these distributions can help to select the events in the experiments. Finally, we show the potential to discover the DM at the 14 TeV LHC, and provide the exclusion limits on the NP scale if this signal is not observed.

Acknowledgments

This work was supported by the National Natural Science Foundation of China, under Grants No. 11021092, No. 10975004 and No. 11135003.

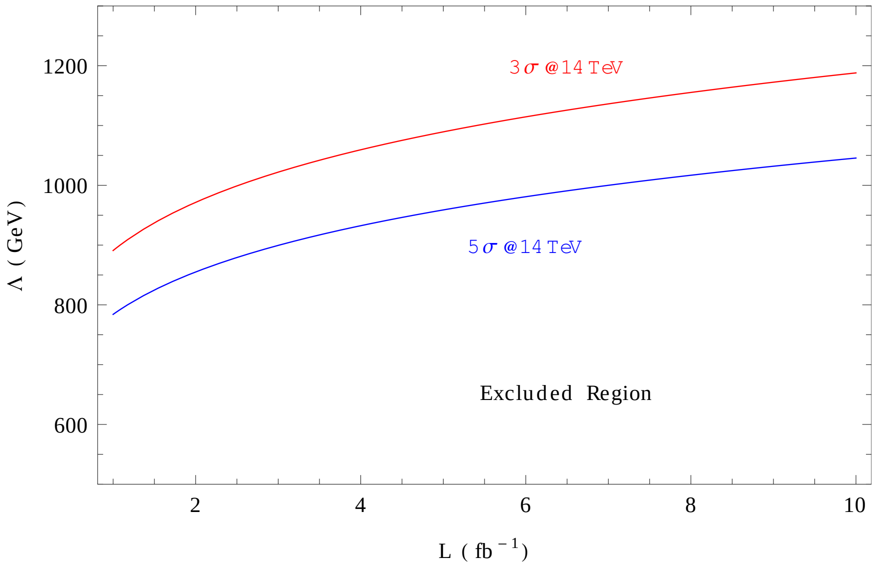

FIG. 20: The limits of the NP scale for 3σ and 5σ exclusions at the LHC with $\sqrt{S} = 14$ TeV, assuming $m = 130$ GeV for the axial-vector operator. We choose the cuts $p_T^{\gamma} > 300$ GeV and $p_T^{miss} > 300$ GeV due to the above analysis of Fig. 14 and Fig. 15.

[1] G. Jungman, M. Kamionkowski, and K. Griest, Phys.Rept. **267**, 195 (1996), hep-ph/9506380.

[2] G. Bertone, D. Hooper, and J. Silk, Phys.Rept. **405**, 279 (2005), hep-ph/0404175.

[3] E. Komatsu et al. (WMAP Collaboration), Astrophys.J.Suppl. **192**, 18 (2011), 1001.4538.

[4] O. Adriani et al. (PAMELA Collaboration), Phys.Rev.Lett. **105**, 121101 (2010), 1007.0821.

[5] J. Chang et al., Nature **456**, 362 (2008).

[6] F. Aharonian et al. (H.E.S.S.), Phys. Rev. Lett. **101**, 261104 (2008), 0811.3894.

[7] A. A. Abdo et al. (The Fermi LAT), Phys. Rev. Lett. **102**, 181101 (2009), 0905.0025.

[8] C. Weniger (2012), 1204.2797.

[9] E. Aprile et al. (XENON100), Phys. Rev. Lett. **105**, 131302 (2010), 1005.0380.

[10] Z. Ahmed et al. (CDMS), Phys. Rev. Lett. **102**, 011301 (2009), 0802.3530.

[11] R. Bernabei et al. (DAMA), Eur. Phys. J. **C56**, 333 (2008), 0804.2741.

[12] C. E. Aalseth et al. (CoGeNT), Phys. Rev. Lett. **106**, 131301 (2011), 1002.4703.

[13] S. Chatrchyan et al. (CMS Collaboration) (2012), 1204.0821.

[14] T. Aaltonen et al. (CDF Collaboration), Phys.Rev.Lett. **108**, 211804 (2012), 1203.0742.

[15] O. Buchmueller et al. (2011), 1106.2529.

[16] T. Li, J. A. Maxin, D. V. Nanopoulos, and J. W. Walker (2011), 1106.1165.

[17] S. Profumo, Phys.Rev. **D84**, 015008 (2011), 1105.5162.

[18] G. Belanger, S. Kraml, and A. Lessa, JHEP **1107**, 083 (2011), 1105.4878.

[19] J. Kile and A. Soni, Phys.Rev. **D84**, 035016 (2011), 1104.5239.

[20] S. Akula, D. Feldman, Z. Liu, P. Nath, and G. Peim, Mod.Phys.Lett. **A26**, 1521 (2011), 1103.5061.

[21] D. Feldman, K. Freese, P. Nath, B. D. Nelson, and G. Peim, Phys.Rev. **D84**, 015007 (2011), 1102.2548.

[22] Y. Bai and H.-C. Cheng, JHEP **06**, 021 (2011), 1012.1863.

[23] I. Gogoladze, R. Khalid, Y. Mimura, and Q. Shafi, Phys. Rev. **D83**, 095007 (2011), 1012.1613.

[24] K. Cheung, K. Mawatari, E. Senaha, P.-Y. Tseng, and T.-C. Yuan, JHEP **10**, 081 (2010), 1009.0618.

[25] J. Goodman et al., Phys. Rev. **D82**, 116010 (2010), 1008.1783.

[26] G. Bertone, D. G. Cerdeno, M. Fornasa, R. Ruiz de Austri, and R. Trotta, Phys. Rev. **D82**, 055008 (2010), 1005.4280.

[27] G. F. Giudice, T. Han, K. Wang, and L.-T. Wang, Phys. Rev. **D81**, 115011 (2010), 1004.4902.

[28] T. Li and W. Chao, Nucl. Phys. **B843**, 396 (2011), 1004.0296.

[29] M. Beltran, D. Hooper, E. W. Kolb, Z. A. C. Krusberg, and T. M. P. Tait, JHEP **09**, 037 (2010), 1002.4137.

[30] H. Zhang, C. S. Li, Q.-H. Cao, and Z. Li, Phys. Rev. **D82**, 075003 (2010), 0910.2831.

[31] N. Arkani-Hamed and N. Weiner, JHEP **12**, 104 (2008), 0810.0714.

[32] D. Fargion, M. Y. Khlopov, R. V. Konoplich, and R. Mignani, Phys. Rev. **D54**, 4684 (1996).

[33] Y. Bai, P. J. Fox, and R. Harnik, JHEP **12**, 048 (2010), 1005.3797.

[34] P. J. Fox, R. Harnik, J. Kopp, and Y. Tsai, Phys.Rev. **D85**, 056011 (2012), 1109.4398.

[35] J. Wang, C. S. Li, D. Y. Shao, and H. Zhang, Phys.Rev. **D84**, 075011 (2011), 1107.2048.

[36] X. Gao, C. S. Li, J. Gao, J. Wang, and R. J. Oakes, Phys.Rev. **D81**, 036008 (2010), 0912.0199.

[37] M. Beltran, D. Hooper, E. W. Kolb, and Z. A. C. Krusberg, Phys. Rev. **D80**, 043509 (2009), 0808.3384.

[38] Q.-H. Cao, C.-R. Chen, C. S. Li, and H. Zhang, JHEP **1108**, 018 (2011), 0912.4511.

[39] N. Jarosik et al., Astrophys. J. Suppl. **192**, 14 (2011), 1001.4744.

[40] E. W. Kolb and M. S. Turner, Front.Phys. **69**, 1 (1990).

[41] B. W. Harris and J. F. Owens, Phys. Rev. **D65**, 094032 (2002), hep-ph/0102128.

[42] J. Pumplin et al., JHEP **07**, 012 (2002), hep-ph/0201195.

[43] S. Frixione, Phys. Lett. **B429**, 369 (1998), hep-ph/9801442.

[44] J. M. Campbell, R. K. Ellis, and C. Williams, JHEP **1107**, 018 (2011), 1105.0020.

[45] U. Baur, T. Han, and J. Ohnemus, Phys. Rev. **D57**, 2823 (1998), hep-ph/9710416.

[46] J. Ohnemus, Phys. Rev. **D47**, 940 (1993).

[47] W. Giele, E. N. Glover, and D. A. Kosower, Nucl.Phys. **B403**, 633 (1993), hep-ph/9302225.

[48] U. Baur and E. L. Berger, Phys. Rev. **D47**, 4889 (1993).